Satellite synthetic aperture radar detection of Delaware Bay plumes: Jet-like feature analysis

Quanan Zheng,[1] Pablo Clemente-Colón,[2] Xiao-Hai Yan,[3] W. Timothy Liu,[4] and Norden E. Huang[5]

Received 18 August 2003; revised 5 November 2003; accepted 14 January 2004; published 19 March 2004.

[1] From the physics of radar imaging of ocean surface processes a theoretical model for the radar imaging of an ocean jet was derived. The theoretical model predicts that the jet current structure, $\mathrm{sech}^2\eta$, constitutes a determining factor for the radar image. The modeled image intensity depends on the axial velocity, decreasing as x^{-1} along the jet axis, and is sensitive to the wind direction with respect to the jet axis. The model was used to interpret synthetic aperture radar (SAR) images of Delaware Bay plumes taken by the RADARSAT-1 (Canadian Radar Satellite) and ERS-2 (European Remote Sensing satellite) satellites during a period from summer 1996 to spring 1997. In all seasons the low-salinity plumes appear as relatively bright, jet-like patterns on SAR images. From a morphological interpretation of the image features, both summer and winter plumes can be divided into three sections along the axis: source, jet, and dispersion region. Along the transverse direction, SAR image interpretations indicate that the plumes have a twin jet structure, which conforms to decomposition of field measurements. In summer the typical axial velocity is estimated at 6×10^{-1} m s^{-1} with a Reynolds number of 18. At about 5 km downstream from the source the plume behaves like a turbulent jet, and beyond that range down to about 10 km downstream, it behaves like a laminar jet. In winter the plumes become weaker than in summer. The typical axial velocity is estimated at 4×10^{-1} m s^{-1} with a Reynolds number of 3. The jet behaves like the laminar jet off the source down to about 4 km downstream. In both summer and winter cases the SAR images were taken at maximum flood tide, and the plumes appeared as jets. In the spring case the SAR image was taken at early flood tide; the plume appeared as an integrated body with relatively uniform bright tunes. In all cases the plume disperses within about 25 km downstream. *INDEX TERMS:* 4235 Oceanography: General: Estuarine processes; 4528 Oceanography: Physical: Fronts and jets; 4546 Oceanography: Physical: Nearshore processes; 4568 Oceanography: Physical: Turbulence, diffusion, and mixing processes; *KEYWORDS:* Delaware Bay, estuarine plume, radar image

Citation: Zheng, Q., P. Clemente-Colón, X.-H. Yan, W. T. Liu, and N. E. Huang (2004), Satellite synthetic aperture radar detection of Delaware Bay plumes: Jet-like feature analysis, *J. Geophys. Res.*, *109*, C03031, doi:10.1029/2003JC002100.

1. Introduction

[2] Estuary plumes are formed by outflows of low-salinity water into the coastal ocean. Delaware Bay plumes have been investigated by using field observations since early 1990s. *Garvine* [1991] discovered that lighter water outflow from Delaware Bay constitutes a source of the Delaware coastal current. *Münchow et al.* [1992] studied subtidal currents at the Delaware Bay mouth region and found a narrow, baroclinic, subtidal jet exiting on the right looking seaward. *Sanders and Garvine* [1996] observed a twin front feature of Delaware Bay plumes. These previous investigations have revealed general features of Delaware Bay plumes. However, the fine structure, detailed dynamic features, and seasonal variability of the plumes have not been completely understood yet because of limited spatial resolutions and limited field observations.

[3] Satellite images may serve as a complementary information source for detecting the fine structure of estuary plumes. Changes in water color, temperature, and salinity between plumes and surrounding waters are easily detected by various remote sensors onboard satellites [*Clemente-Colón*, 2001]. Among these sensors, synthetic aperture radar (SAR) has unique advantages to be used for detecting estuary plumes. Besides all weather and all day detecting abilities, SAR images are characterized by high spatial resolutions and the sensitivity to

[1]Department of Meteorology, University of Maryland, College Park, Maryland, USA.
[2]NOAA/NESDIS, Camp Springs, Maryland, USA.
[3]College of Marine Studies, University of Delaware, Newark, Delaware, USA.
[4]Jet Propulsion Laboratory 300-323, California Institute of Technology, Pasadena, California, USA.
[5]Ocean and Ice Branch, NASA Goddard Space Flight Center, Greenbelt, Maryland, USA.

0148-0227/04/2003JC002100$09.00

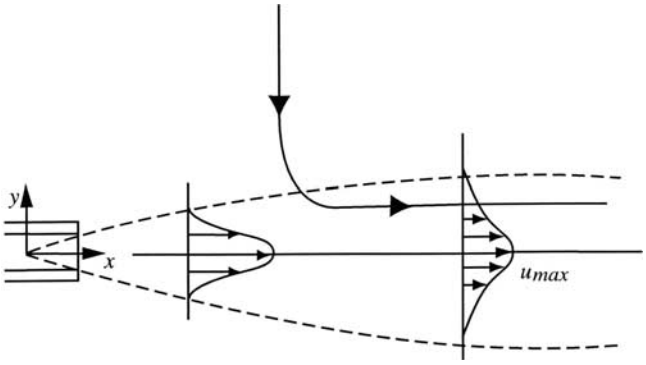

Figure 1. A scheme of a two-dimensional jet flow.

the ocean dynamic processes. The state-of-the-art resolution of satellite SAR images may reach about 10 m, which is suitable for observations of two-dimensional structure with a scale larger than 100 m. In principle, satellite SAR also has a potential to indirectly detect ocean water salinity variation [*Clemente-Colón*, 2001] as well as ocean current variability [*Zheng et al.*, 1998, 2001], which are the major features of estuary plumes. In this study, we use the RADARSAT and ERS-2 satellite SAR images to detect the Delaware Bay plumes. Through image morphological interpretation and data analysis, the fine structure, dynamic features, and seasonal variability of the plumes are obtained.

[4] The next section gives the derivation of an analytical model for a SAR-imaged ocean jet. Satellite data and field observations used for this study are described in section 3. The results of interpretation of satellite SAR images of Delaware Bay plumes collected during a period from summer 1996 to spring 1997 are given in section 4. Section 5 includes discussion and major conclusions.

2. Theoretical Model of a Jet SAR Image

2.1. Two-Dimensional Jet

[5] A two-dimensional jet is a special flow formed by an efflux of a fluid from a long and narrow orifice into the same type of fluid as the jet itself, as illustrated in Figure 1 [*Kundu*, 1990]. Dynamically, the jet is controlled by two conditions. One is the momentum flux preservation,

$$M = \rho \int_{-\infty}^{\infty} u^2 dy = \textit{independent of } x, \tag{1}$$

where ρ is the fluid density, u is the velocity x component, and the coordinate system is shown in Figure 1. The other condition is a similarity solution of the stream function in the form of

$$\psi = ax^{1/3} \tanh \eta, \tag{2}$$

where

$$a = \left(\frac{9A_H M}{2\rho}\right)^{1/3}. \tag{3}$$

Here A_H is the horizontal eddy viscosity, and

$$\eta = \frac{y}{bx^{2/3}}, \tag{4}$$

in which

$$b = \left(\frac{48A_H^2\rho}{M}\right)^{1/3}. \tag{5}$$

From equation (2) we derived the velocity components of the jet. The x component or axial velocity is given by

$$u = u_{\max} \sec h^2 \eta, \tag{6}$$

where $u_{\max}$ is the maximum axial velocity at the center of the jet, given by

$$u_{\max} = \frac{a}{b} x^{-1/3} = \left(\frac{3M^2}{32\rho^2\nu}\right)^{1/3} x^{-1/3}. \tag{7}$$

The y component or transverse velocity is given by

$$v = v_{\max}\left(2\eta \sec h^2 \eta - \tanh \eta\right), \tag{8}$$

where $v_{\max}$ is the maximum transversal velocity given by

$$v_{\max} = \frac{a}{3} x^{-2/3}. \tag{9}$$

[6] These equations imply that the dynamics of an ideal two-dimensional jet are characterized by five factors: (1) a jet axis, (2) a jet width that increases as $x^{2/3}$, (3) an x component velocity that decreases as $x^{-1/3}$, (4) a y component that decreases as $x^{-2/3}$, and (5) point $x = 0$ is a singular point.

2.2. General Expressions of a Sea Surface Radar Image

[7] A radar image records a two-dimensional distribution of the intensity of radar return signals. Assuming that the radar receiving system is a perfectly linear system, the intensity of radar return signals should depend linearly on the density of backscatterers of the target, which is quantified by a backscatter cross section per unit area. For an ocean surface, the backscatter cross section per unit area is given by [*Plant*, 1990]

$$\sigma_\circ(\theta)_{ij} = 16\,\pi k_0^4 \left|g_{ij}(\theta)\right|^2 \psi(0, 2k_0 \sin\theta), \tag{10}$$

where θ is the incidence angle, k_0 is the wave number of the radar waves, and ψ is the two-dimensional (Cartesian) wave number spectral density of the ocean surface wave field that satisfies the Brag resonant scatter condition, the incident radiation is in the x-z plane (z is the vertical direction and x, y are the horizontal coordinates), the subscripts ij denote the polarization of the incident and backscattered radiation, respectively, and $g_{ij}(\theta)$ are the first-order scattering coefficients. For horizontal polarization, $g_{ij}(\theta)$ is

$$g_{HH}(\theta) = \frac{(\varepsilon_r - 1)\cos^2\theta}{\left[\cos\theta + \left(\varepsilon_r - \sin^2\theta\right)^{1/2}\right]^2}, \tag{11}$$

and for vertical polarization, $g_{ij}(\theta)$ is

$$g_{VV}(\theta) = \frac{(\varepsilon_r - 1)\left[\varepsilon_r\left(1 + \sin^2\theta\right) - \sin^2\theta\right]\cos^2\theta}{\left[\varepsilon_r\cos\theta + \left(\varepsilon_r - \sin^2\theta\right)^{1/2}\right]^2}, \tag{12}$$

where ε_r is the relative dielectric constant of seawater [*Saxton and Lane*, 1952; *Klein and Swift*, 1977].

[8] From equation (10) one can see that the two-dimensional wave number spectral density of the ocean surface wave field is a definitive factor for the intensity of the radar return signals if the radar wave number and the incidence angle are given. In that case, the intensity variability on radar images, i.e., the so-called image patterns or signatures, will depend only on the spatial variability of ψ.

2.3. Jet Modulation to Wave Spectra

[9] On the assumption that the high-frequency band of the wave spectrum is in the equilibrium state, i.e., the wave spectrum does not change with time, and is spatially uniform, *Yuan* [1997] derived the wave number spectral density of the high-frequency ocean surface wave field for gravity-capillary wave band (for C band SAR) in the form of

$$\psi = m_3^{-1}\left[m\left(\frac{u_*}{c}\right)^2 - 4\gamma k^2\omega^{-1} - S_{\alpha\beta}\frac{\partial U_\beta}{\partial x_\alpha}\omega^{-1}\right]k^{-4}. \tag{13}$$

In the above, m and m_3 are coefficients, u_* is the friction velocity, c is the wave phase speed, γ is the viscosity of seawater, ω is the angular frequency of the ocean surface waves, k is the wave number of ocean surface waves, and the scalar product of the excess momentum flux tensor and the modification velocity tensor is given by

$$S_{\alpha\beta}\frac{\partial U_\beta}{\partial x_\alpha} = \left[\frac{\partial u}{\partial x}\cos^2\phi + \left(\frac{\partial u}{\partial y} + \frac{\partial v}{\partial x}\right)\cos\phi\sin\phi + \frac{\partial v}{\partial y}\sin^2\phi\right]/2. \tag{14}$$

Here, u and v are velocity components, and φ is the wave direction with respect to x axis, if the effects of the long ocean waves are ignored. In our case, the three SAR images used for the analysis were taken at very low sea state with the wave height of 1.86 m, 0.55 m, and 0.89 m as listed in Table 1. Therefore it is an acceptable approximation if we assume that the effects of the ocean wave field on SAR imaging are negligible. We rechecked Yuan's derivation, and found that equation (13) approximately stands if and only if the length-scale ratios satisfy the following relationship

$$\left(\frac{l}{L_1}, \frac{l}{L_2}, \frac{l}{L_3}\right) \prec\prec 1, \tag{15}$$

where l represents a length scale required by statistical significance of the spectra, which should be greater than 5 m (100 waves) for gravity-capillary wave band, L_1, L_2, and L_3 are the length scales of the wind field, the viscosity variation, and the current field, respectively.

[10] Equation (13) may further be rewritten in the form of three components, i.e.,

$$\psi = \psi_1 + \psi_2 + \psi_3. \tag{16}$$

Table 1. Information and Parameters of SAR Images Used for This Study and Field Data at the Imaging Time

Codes	96813	97207	97514
Satellite	RADARSAT-1	RADARSAT-1	ERS-2
Orbit direction	descending	descending	descending
Time, UTC	13 Aug. 1996, 1107	7 Feb. 1997, 1115	14 May 1997, 1543
Beam mode	SWB	SWB	Standard
Resolution, m	100 × 100	100 × 100	30 × 26.3
Swath, km	450	450	100
Tidal phase	maximum flood	maximum flood	early flood
Wind speed, m s^{-1}	9.2	3.9	5.1
Wind direction	180°	335°	185°
Wave height, m	1.86	0.53	0.89
Dominant WAVE Period, s	5.88	9.09	8.33
Mean wave dir.	123°	118°	143°
Air temperature, °C	23.5	N/A	13.4
Water temperature, °C	22.7	5.9	12.1

The first component

$$\psi_1 = m_3^{-1}m\left(\frac{u_*}{c}\right)^2 k^{-4} \tag{17}$$

represents the wind input. The second component

$$\psi_2 = -4m_3^{-1}\gamma k^{-2}\omega^{-1} \tag{18}$$

represents the dissipation induced by the viscosity. The third component

$$\psi_3 = -m_3^{-1}S_{\alpha\beta}\frac{\partial U_\beta}{\partial x_\alpha}\omega^{-1}k^{-4} \tag{19}$$

represents modulation induced by a spatially variable current. In our case, the spatially variable current is the two-dimensional jet. Substituting equations (6), (8), and (14) into equation (19) yields

$$\psi_3 = -m_3^{-1}\omega^{-1}k^{-4} \cdot \begin{bmatrix} -\frac{a}{6b}x^{-4/3}\left(\cos^2\phi + 2x^{-1}y\cos\phi\sin\phi - \sin^2\phi\right)\sec h^2\left(\frac{y}{bx^{2/3}}\right) \\ +\frac{2a}{3b^2}x^{-2}\left(y\cos^2\phi - \frac{3}{2}x\cos\phi\sin\phi + \frac{2}{3}x^{-1}y\cos\phi\sin\phi - \sin^2\phi\right) \\ \cdot\sec h^2\left(\frac{y}{bx^{2/3}}\right)\tanh\left(\frac{y}{bx^{2/3}}\right) \\ +\frac{a}{9}x^{-5/3}\cos\phi\sin\phi\tanh\left(\frac{y}{bx^{2/3}}\right) \end{bmatrix}. \tag{20}$$

Substituting equation (20) into equation (10) yields the backscatter cross section per unit area induced by the two-dimensional jet

$$\sigma_\circ(\theta)_{ij,jet} = -16\pi k_0^4\left|g_{ij}(\theta)\right|^2 m_3^{-1}\omega^{-1}k^{-4} \cdot \begin{bmatrix} -\frac{a}{6b}x^{-4/3}\left(\cos^2\phi + 2x^{-1}y\cos\phi\sin\phi - \sin^2\phi\right)\sec h^2\left(\frac{y}{bx^{2/3}}\right) \\ +\frac{2a}{3b^2}x^{-2}\left(y\cos^2\phi - \frac{3}{2}x\cos\phi\sin\phi + \frac{2}{3}x^{-1}y\cos\phi\sin\phi - \sin^2\phi\right) \\ \cdot\sec h^2\left(\frac{y}{bx^{2/3}}\right)\tanh\left(\frac{y}{bx^{2/3}}\right) + \frac{a}{9}x^{-5/3}\cos\phi\sin\phi\tanh\left(\frac{y}{bx^{2/3}}\right) \end{bmatrix} \tag{21}$$

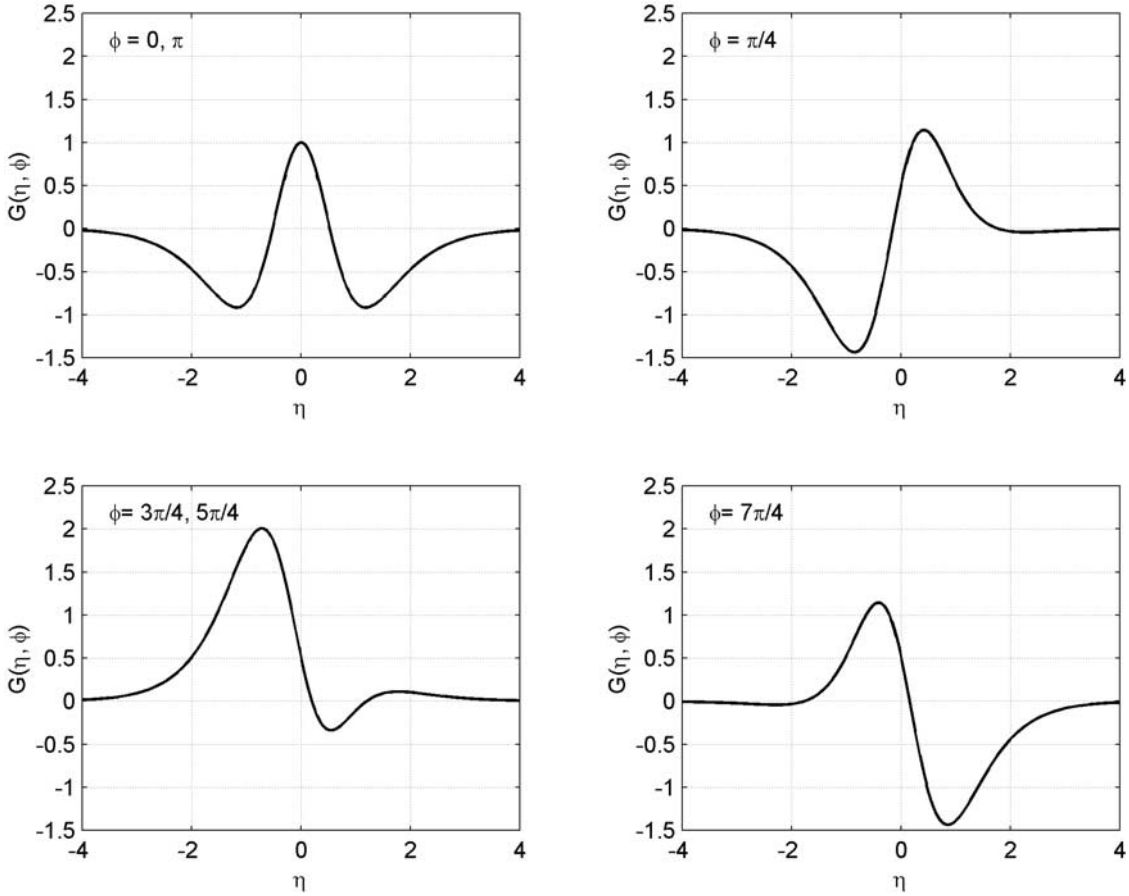

Figure 2. Theoretical models of normalized radar image intensity (or gray level) structure along the transverse section through a point on the jet axis for $x = b^3$. The wind direction with respect to the jet axis is given at the left upper corner in each case.

This is a theoretical model for a radar image of two-dimensional jet. One can see that the image depends not only on the structure of jet current field, but also on the wind direction (In the case of gravity-capillary waves, the wave direction is consistent to the sea surface wind direction).

[11] In order to simplify the analysis without loss of physics and the major features of the jet radar image, we derived an approximate form of equation (21) from an assumption that the y component velocity, v, is negligible in comparison with the x component (In fact, this condition stands in most cases.). Thus we have

$$\sigma_\circ(\theta)_{ij,jet} = -16\pi k_0^4 \left|g_{ij}(\theta)\right|^2 m_3^{-1}\omega^{-1}k^{-4}\cdot\left\{\frac{u_{\max}}{6}x^{-1}\left[\cos^2\phi + \left(4\eta\cos\phi - \frac{6x^{1/3}}{b}\sin\phi\right)\cos\phi\tanh\eta\right]\sec h^2\eta\right\}, \tag{22}$$

where η is given by equation (4). This theoretical model predicts that the jet radar image has three major features. First, the jet current structure, $\mathrm{sech}^2\eta$, constitutes a determinant factor for its radar image. Second, the image intensity depends on the maximum x component of velocity and decreases as x^{-1} along the jet axis. Third, the image intensity is sensitive to the wind direction with respect to the jet axis. The jet may even become invisible on radar images for wind direction $\phi = \pi/2, 3\pi/2$.

[12] In order to examine effects of the wind direction on radar imaging of the jet, we further define *function* $G(\eta, \varphi)$ as

$$G(\eta,\phi) = \left[\cos^2\phi + \left(4\eta\cos\phi - \frac{6x^{1/3}}{b}\sin\phi\right)\cos\phi\tanh\eta\right]\sec h^2\eta. \tag{23}$$

The physical meaning of $G(\eta, \varphi)$ is the dimensionless radar backscatter section of a two-dimensional jet. We plotted the curves of $G(\eta, \varphi)$ versus η for $x = b^3$ and for typical values of φ, which are shown in Figure 2. These curves represent theoretical models of normalized radar image intensity (or gray level) patterns along the transverse section through a point on the jet axis at $x = b^3$ for various wind directions. One can see that in all cases, G varies with η and has only one positive peak, which is accompanied by one negative peak (two negative peaks for $\varphi = 0, \pi$). The case for $\varphi = 0, \pi$ is the only case in which the $G(\eta, \varphi)$ versus η curve is symmetric about the x axis ($\eta = 0$). In all other cases, the positive peaks shift off the x axis either rightward (for $\varphi = \pi/4$) or leftward (for $\varphi = 3\pi/4$, $5\pi/4$, and $7\pi/4$), implying that the locations of peak intensity values of the jet radar

image would not coincide with the jet axis, which is the location of the maximum x component velocity.

3. Data

3.1. Satellite SAR Images

[13] The SAR images used for this study were taken by the RADARSAT-1 and the ERS-2 (European Remote Sensing) satellites. RADARSAT-1 was launched in 1995. RADARSAT-1 SAR operates at a C band (5.3 GHz) microwave wavelength (5.6 cm) with HH antenna polarization. RADARSAT-1 SAR is characterized by multiple antenna beam modes. With a total of 14 modes, this radar generates images with different resolutions and different swath widths. The images we used were generated in ScanSAR Wide mode B (SWB) with a nominal resolution of 100 m and a swath width of 450 km. The SAR aboard ERS-2, launched in 1991, also operates at a C band (5.3 GHz) microwave wavelength but with a VV antenna polarization. The antenna has only one beam mode, which generates images with a nominal resolution of 30 m along track by 26.3 m across track and a swath width of 100 km [*Clemente-Colón*, 2001]. The SAR images used for this study were acquired during a period from summer 1996 to spring 1997. The main information and parameters of the images are listed in Table 1.

3.2. Field Data

[14] We used in situ measurements published by *Sanders and Garvine* [1996] to determine the salinity distribution and current field structure of a low-salinity estuary plume off the Delaware Bay. The original data were measured with conductivity-temperature-depth (CTD) along transect line labeled AA in Figure 3 on 28 and 29 May and 25 June 1992. We used density anomaly (ρ_t) data derived from the measurements to calculate the current field structure. If we assume that the y component of velocity is again negligible, the water density anomaly should depend on fresh water outflow. After simple derivation, the following approximate relation stands

$$\rho_t = -\alpha u(y), \tag{24}$$

where α is a constant to be determined, and $u(y)$ represents the x component of velocity. This means that using density anomaly data we may determine a normalized form of function of $u(y)$ used for dynamical analysis even though α is unknown.

[15] From equations (13), (14), and (24), one can see that simultaneously measured winds are necessary data for SAR image interpretation. Fortunately, there is a NOAA Delaware Bay Buoy (ID: 44009, location: 38°27′49″N 74°42′07″W) available near our study area (15 km southeast). We used continuous winds measured by the buoy at a height of 5 m above the sea level to represent the sea surface winds in the plume region. We also used the ocean surface wave data measured by the Buoy for the sea state analysis.

[16] The tides are another important dynamic element, which may have influence on the SAR imaging of the estuary plumes. We consulted data available at the Website http://tidesonline.nos.noaa.gov/ (Center for Operational Oceanographic Products and Services, Tides Online, NOAA National Ocean Service, Silver Spring, Maryland, 2004, hereinafter referred to as Center for Operational Oceanographic Products and Services, 2004) to determine the tide phase at the SAR imaging time.

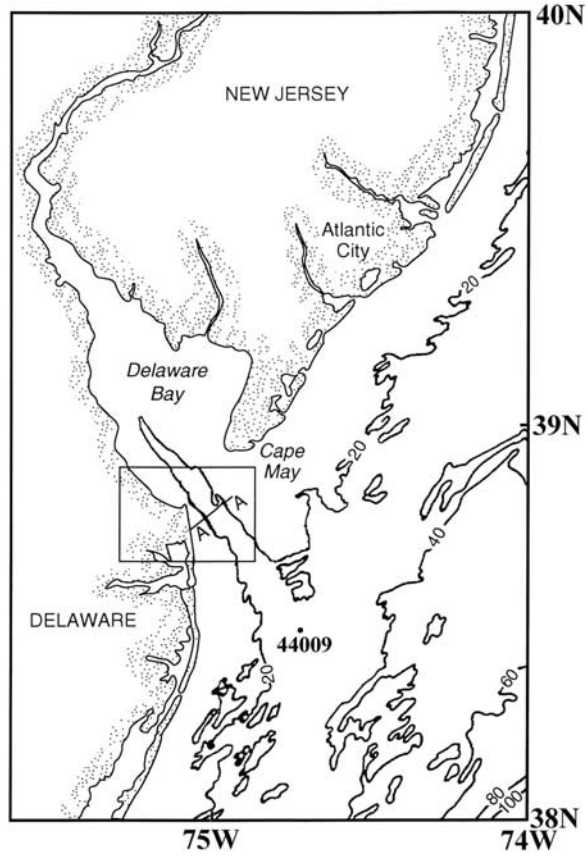

Figure 3. A map of the Delaware Bay area. A rectangular box marked at the bay mouth shows the study area, in which transect line AA shows the locations of field data measured by *Sanders and Garvine* [1996] that are shown in Figure 4. Point 44009 shows a location of the NOAA Delaware Bay Buoy, from which we obtained simultaneous field measurements at SAR imaging time.

4. Interpretations of SAR Images of Delaware Bay

4.1. Study Area

[17] The Delaware Bay is located on the east coast of the United States as shown in Figure 3. The total surface area of the bay is about 1864 km^2. The south-north length of the bay is about 75 km, and the east-west breadth varies from 18 km at the mouth from Cape Henlopen, Delaware to Cape May, New Jersey to a maximum of 45 km at the broadest point [*Polis and Kupferman*, 1973; *Zheng et al.*, 1993]. The Delaware Bay plume originates at the bay mouth and extends offshore along a deep channel, which has a maximum depth of over 20 m and the width at the bay mouth of about 3 km, up to about 20 km downstream onto the continental shelf [*Wong and Münchow*, 1995; *Sanders and Garvine*, 1996].

[18] The Delaware Estuary plumes, in fact, are an outflow of low-salinity estuarine water from the bay. The measure-

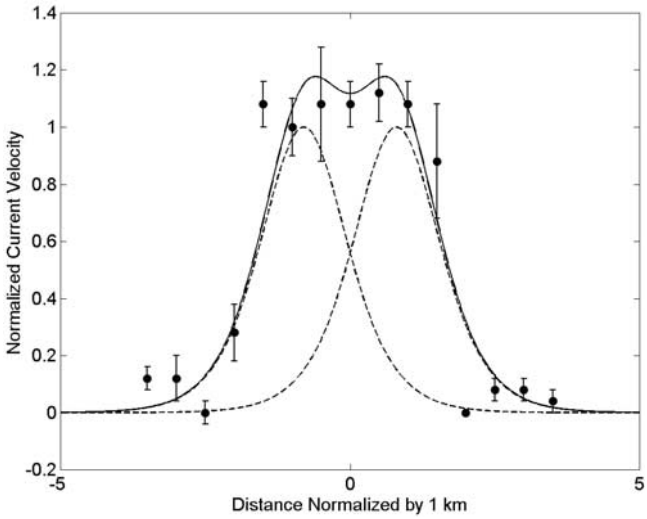

Figure 4. A twin jet structure model of the Delaware Bay plume current field. Data points are derived from the density anomaly data measured along transect AA in Figure 3 [*Sanders and Garvine*, 1996, Figure 4]. Dashed line shows two model jet current fields symmetric about the jet axis or central point. Solid line shows a composite of the two jet current fields.

ments along transect line AA marked in Figure 3 by *Sanders and Garvine* [1996] indicated the salinity inside the plume is 2–3 psu lower than that of surrounding shelf water. From the measurements, they determined that the width of the plume is about 4 km, and the depth is about 5 m. They also found that the plume has a twin front structure. The onshore and offshore fronts lie at about 1 km and 5 km from the Delaware coast, respectively. Using the density anomaly data [*Sanders and Garvine*, 1996, Figure 4] and relation (24), we calculated the current field structure along transect AA, shown in Figure 4. One can see that we may treat the current field of the plume as two jet current fields, which are symmetric about the central point. We call this kind of the plume current field a twin jet structure.

[19] The field-based investigations have revealed basic features of the physical oceanography in the study area. Owing to the limited temporal and spatial resolutions of field measurements, however, the physical nature, dynamical features, and the fine structure of the estuary plumes with a spatial resolution up to 10 m are still not clear enough. Motivation of this effort is to fill these gaps with the data and information extracted from high-resolution SAR images. Following are the results obtained by interpretations of three cases, which occurred in summer, winter, and spring, respectively.

4.2. Summer Case

[20] In summer, June, July, and August, southerly winds prevail in the region. Southerly alongshore winds produce an Ekman offshore surface drift. This Ekman divergent flow is compensated by an onshore deeper flow that brings colder water to the surface forming coastal upwelling. Therefore the local summer is also called ''upwelling favorable season'' [*Münchow and Garvine*, 1993b]. The river discharge is minimum during the summer and reaches maximum during spring. Figure 5 shows a RADARSAT-1 SWB image covering the Delaware Bay mouth region taken on 13 August 1996, 1107 UTC. We code the image by identification number 96813 and list the major specifications in Table 1. The time series vector wind records measured by NOAA Delaware Bay Buoy 44009 gave the wind speed as 9.2 m s^{-1} and the wind direction as 180° at the SAR imaging time. The tide phase was at maximum flood.

[21] The bright area on the lower left of the image is land, part of the coastal region of southern Delaware. To the right, there is a light bright, plume-like pattern. On the basis of the known general features of the Delaware Estuary Plumes derived from field measurements, as shown by *Münchow and Garvine* [1993b, Figure 9] and *Sanders and Garvine* [1996, Figure 5], we interpret this imagery pattern as a signature of the Delaware Estuary Plume. The surrounding dark areas are the coastal waters, the Delaware Bay on the upper left, the Atlantic Ocean on the right, and the Rehoboth Bay on the lower left. The main features of the image are drawn on the map shown in Figure 6. One can see that the axis of plume takes an angle of 23° with the coastline, which is close to the direction of the deep channel (30° with the coastline), but turns right 7° toward a longshore direction. The plume has twin image fronts corresponding to the twin jet structure as shown in Figure 4. Along the axis, we divided the plume into three sections: the source section characterized by an almost unchanged transverse width of 3.0 km, the jet section characterized by a gradually expanding width with a maximum value of 7.7 km, and the dispersion section characterized by a gradually shrinking width and vague imagery. The observed total length of the plume is 21.3 km, of which the length of the jet section is about 11.0 km.

[22] Comparing the image fronts in Figures 5 and 6 to the envelope curves of two-dimensional jet in Figure 1, one can see there is a similarity between the two. In order to prove

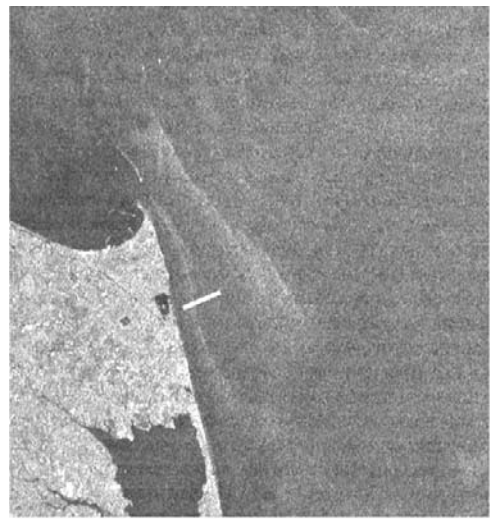

Figure 5. A RADARSAT-1 SWB image covering the Delaware Bay mouth region taken on 13 August 1996, 1107 UTC. The white line represents the transect along which gray level values are taken for comparison to the theoretical model.

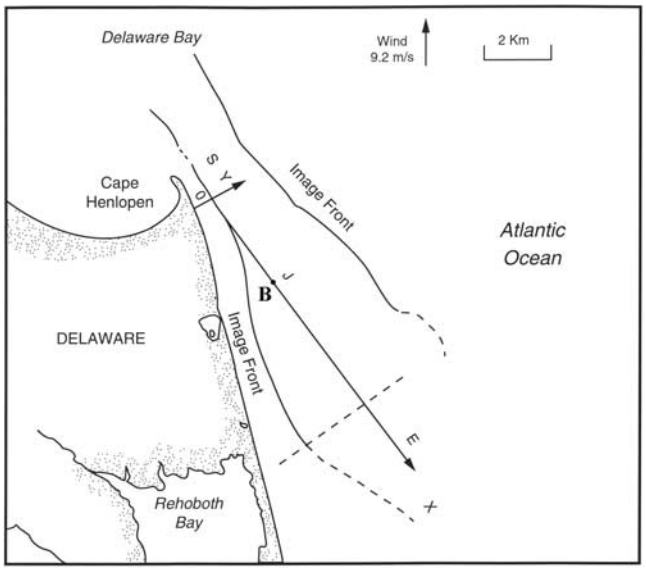

Figure 6. An interpretation map of Figure 5. S, J, and E represent the source, jet, and extension sections of the jet, respectively. B is the point we used to estimate the axial velocity.

their physical identity, however, we need further evidence. For this reason, we performed three tests discussed next.

4.2.1. Transverse Structure of the Image Front

[23] If we assume that a linear function is used for conversion of the radar backscatter section to the gray level on the SAR image, then it is reasonable to use a normalized gray level curve to represent the spatial structure of dimensionless radar backscatter section. For the two-dimensional jet, we have derived the theoretical model of dimensionless radar backscatter section as equation (23) and plotted the curves for typical wind directions as shown in Figure 2. On the other hand, we took transect of the image front along the white line marked in Figure 5. We plotted the normalized gray level values measured along transect (data points) and the theoretical model curve for $\varphi = 3\pi/4$ in Figure 7. One can see that the model curve fits the data points quite well. Both of them are characterized by a positive peak shifting off the x axis rightward, which is a unique response of SAR imaging to the wind direction derived from this study. This means that the ocean process that generates the image front has the transverse structure identical or similar to the two-dimensional jet.

4.2.2. Spreading of the Image Front

[24] From the image shown in Figure 5, we can see that the image front spreads within the jet section. We measured the spreading process of the image front representing a streamline with respect to the axis, which is an extension line of the image front in the source section. We plotted the measured data as solid points in Figure 8. The solid straight line represents a linear relation

$$y = -0.40x. \tag{25}$$

This relation represents width spreading of a turbulent jet [*Kundu*, 1990]. The dashed line represents a relation

$$y = -0.72x^{2/3}. \tag{26}$$

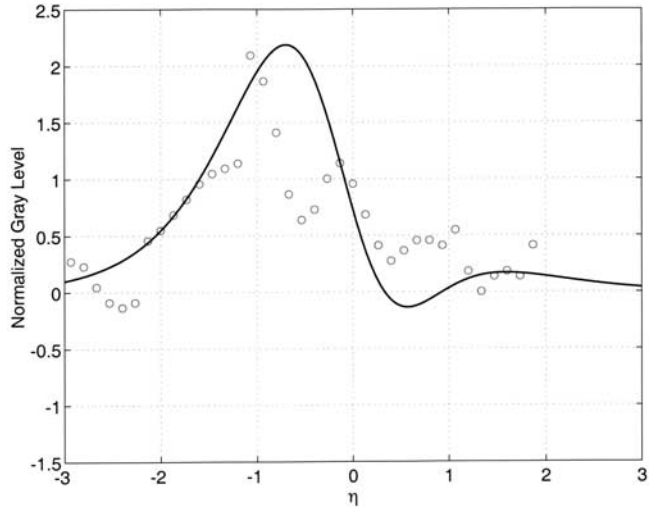

Figure 7. Comparison of normalized gray level values measured along the transect marked in Figure 5 (data points) and the theoretical model curve for $\varphi = 3\pi/4$.

This relation represents width spreading of a laminar jet [*Kundu*, 1990]. One can see that from 0 to 6 km, the turbulent jet gives an excellent description of width spreading of the plume, and beyond that the laminar jet does better job than the turbulent jet.

4.2.3. Estimates of Axial Velocity and Reynolds Number

[25] From theories of the two-dimensional jet, we derived a theoretical model for the axial velocity. Substituting equation (6) into equation (1) and computing the integration yield

$$M = \frac{4}{3} b\rho x^{2/3} u_{\max}^2. \tag{27}$$

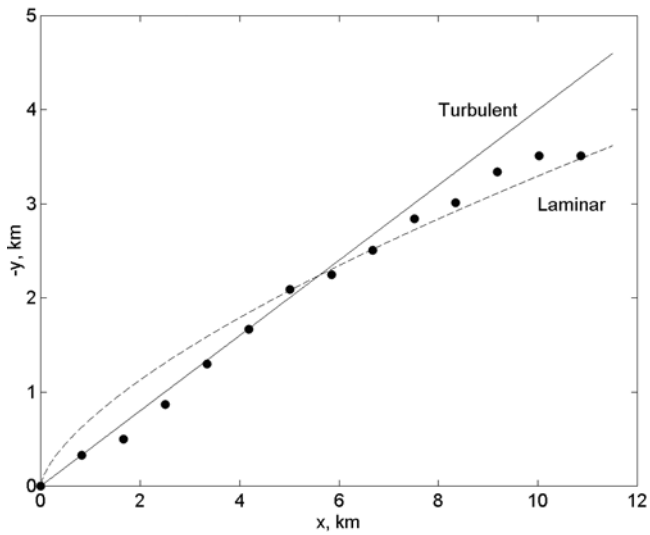

Figure 8. Comparison of the spreading process of the image front with respect to the axis to theoretical models. Data points are taken from J section on Figure 6. The solid line represents width spreading of a turbulent jet. The dashed line represents width spreading of a laminar jet.

Substituting equation (27) into equation (7) yields

$$u_{\max} = \frac{6A_H}{b^2 x^{1/3}}. \quad (28)$$

This relation indicates that if the eddy viscosity A_H is reasonably chosen, and the parameter b is determined from the SAR image, the maximum axial velocity at a given point on the x axis can be calculated. In our case, from the SAR image shown in Figure 5, we have $y = 2.1$ km for $x = 5.0$ km (point B in Figure 6). From Figure 7 we know that the position of the peak gray level corresponds to $\eta = 0.676$. Substituting these values into equation (4) yields $b = 1.06$ km$^{1/3}$. We choose A_H as 2×10^2 m^2 s^{-1}, a typical value for the upper ocean [*Kundu*, 1990]. From equation (28), we obtain the axial velocity at B

$$u_{\max} = 6 \times 10^{-1} \text{ m s}^{-1}. \quad (29)$$

This value is comparable with field measurements. For example, *Wong and Münchow* [1995] gave ADCP observations collected in the same region and a regular distribution of the largest noise (= Raw data − Mean − Tide) vectors with amplitudes of the order of 60 cm s^{-1} and downstream orientations at the deep channel [see *Wong and Münchow*, 1995, Figure 17c]. We interpret that the noise vectors represent the outflows generated by Delaware Bay plumes, thus it is not surprising that our estimate for the jet axial velocity is consistent with their field measurements. This consistence implies that the two-dimensional jet is a good model for describing the behavior of this estuary plume.

[26] Furthermore, from the data points shown on the Figure 8, we determine the length scale of the plume as 6 km. Therefore we obtain that an estimate of the Reynolds number R_e ($=UL/A_H$) is 18, implying a relatively strong jet.

4.3. Winter Case

[27] In winter, December through February, northerly winds prevail. Northerly alongshore winds produce an Ekman onshore surface drift. Therefore the local winter is also called "downwelling favorable season" [*Münchow and Garvine*, 1993b]. The river discharges in winter is below the peak phase. Figure 9 shows a RADARSAT-1 SWB image covering the Delaware Bay mouth region taken on 7 February 1997, 1115 UTC. We code the image by identification number 97207 and list the major specifications in Table 1. Buoy 44009 gave the wind speed as 3.9 m s^{-1} and the wind direction as 335° at the SAR imaging time. The tide phase was at maximum flood.

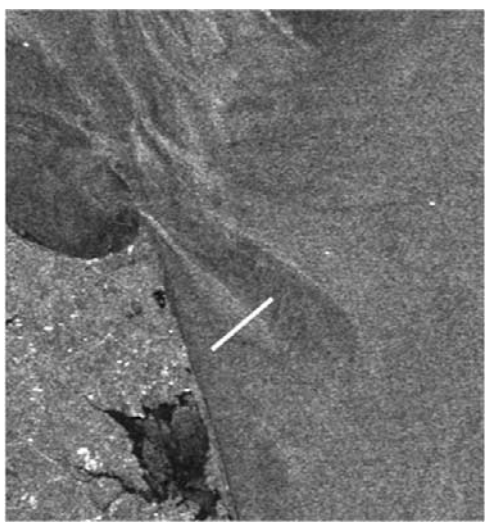

Figure 9. A RADARSAT-1 SWB image covering the Delaware Bay mouth region taken on 7 February 1997, 1115 UTC. The white line represents the transect along which gray level values are taken for comparison to the theoretical model.

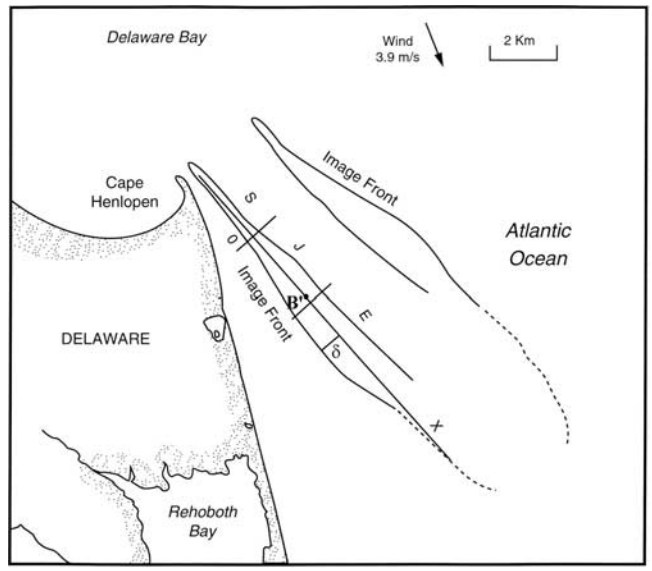

Figure 10. An interpretation map of Figure 9. S, J, and E represent the source, jet, and extension sections of the jet, respectively. B′ is a point we used to estimate the axial velocity.

[28] On the image, the bright area on the lower left is the coastal region of southern Delaware. Just to the right, there is a light bright, plume-like imagery, which is interpreted as a signature of the Delaware Estuary Plume. Figure 10 provides an interpretation map of the image. The axis of plume takes an angle of 26° with the coastline, which is found 3° more offshore than that in summer case. The axial direction of the plume is also close to the direction of the deep channel (30° with the coastline), but turns right 4° facing downstream direction. The plume also has twin image fronts similar to the twin jet structure as shown in Figure 4. Again, we divided the plume along the axis into three sections: the source section characterized by an almost unchanged transverse width of 3.8 km, the jet section characterized by a gradually expanding width with a maximum value of 6.6 km, and the dispersion section characterized by a gradually shrinking width and vague imagery. The total length of the observed plume feature is 19.7 km, in which the length of the jet section is 4.0 km.

4.3.1. Transverse Structure of the Image Front

[29] In Figure 11, we plotted the normalized gray level values measured along white line transect marked in Figure 9 along with the theoretical model curve for $\phi = 0$. One can see that the model curve fits the data points quite well. Both curves are characterized by a positive peak on the x axis. This verifies again that the ocean process that

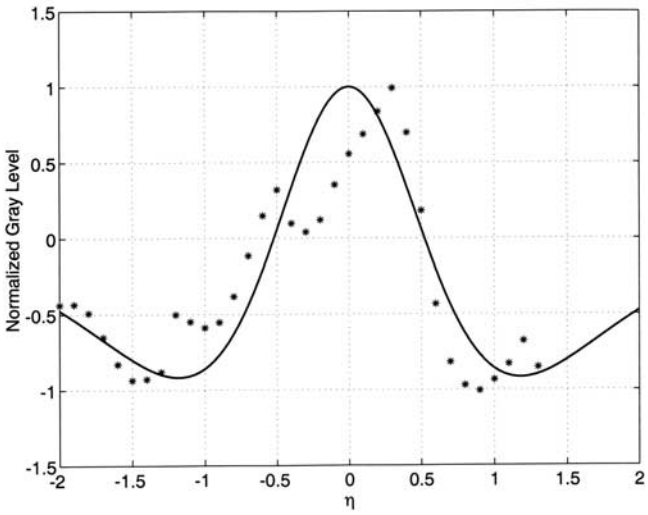

Figure 11. Comparison of normalized gray level values measured along the transect marked in Figure 9 (data points) and the theoretical model curve for $\varphi = 0$.

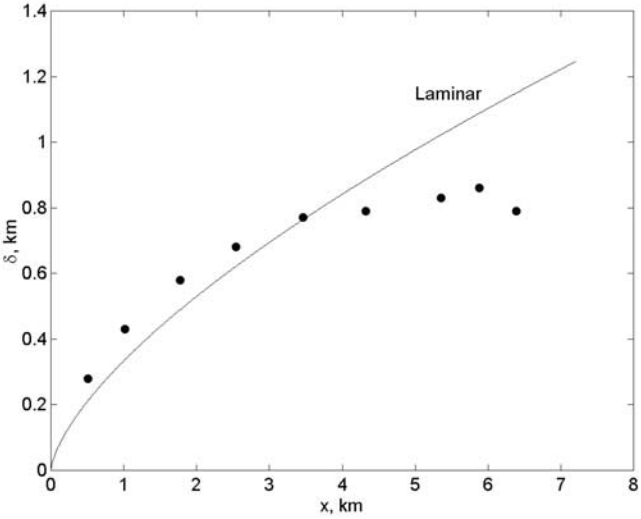

Figure 12. Comparison of the spreading process of the image front with respect to the axis to theoretical models. Data points are taken from J section on Figure 10. The dashed line represents width spreading of a laminar jet.

generates the image front has the transverse structure identical to the two-dimensional jet.

4.3.2. Spreading of the Image Front

[30] From the image shown in Figure 9, one can see that the front spreads once again within the jet section. We measured the front spreading with respect to the axis and plotted these values in Figure 12. The solid curve in the figure represents a relation given by

$$\delta = 0.334x^{2/3}. \tag{30}$$

This equation represents the width spreading of a laminar jet [*Kundu*, 1990].

4.3.3. Estimates of Axial Velocity and Reynolds Number

[31] We can also estimate the maximum axial velocity at a given point on the x axis. For example, for point B′ in Figure 10, we have $y = 0.77$ km for $x = 3.5$ km, implying $b\eta = 0.33$. For this relatively weak plume, we assume that the observed position of the boundary corresponds to $\eta = 0.2$. Substituting these values into equation (4) yields $b = 1.65$ km$^{1/3}$. From equation (28) and choosing A_H as 2×10^2 m^2 s^{-1} again, we obtain an axial velocity at B′ of

$$u_{\max} = 4 \times 10^{-1} \text{ m s}^{-1}. \tag{31}$$

[32] Furthermore, from the data plotted in Figure 12 we determine the length scale of the plume as 1.5 km. Therefore we obtain an estimate of the Reynolds number R_e of 3, implying a relatively weak jet.

4.4. Spring Case

[33] In spring, March through May, the winds are in a transit period from winter to summer. The river discharge is in the peak phase, particularly in April and May. Figure 13 shows an ERS-2 SAR image of the Delaware Bay mouth region taken on 14 May 1997, 1543 UTC. We code the image by identification number 97514 and list the major specifications in Table 1. Buoy 44009 registered a wind speed of 5.1 m s^{-1} and a wind direction of 185° at the SAR imaging time. The tide phase was at early flood.

[34] The bright area on the lower left side of the image is the coastal region of southern Delaware. To the right, there is a light bright, plume-like feature, which is interpreted as a signature of the Delaware Estuary Plume. The plume has twin image fronts corresponding to the twin jet structure shown in Figure 4. The total length of the plume is about 23.1 km. According to the imagery features, the plume can

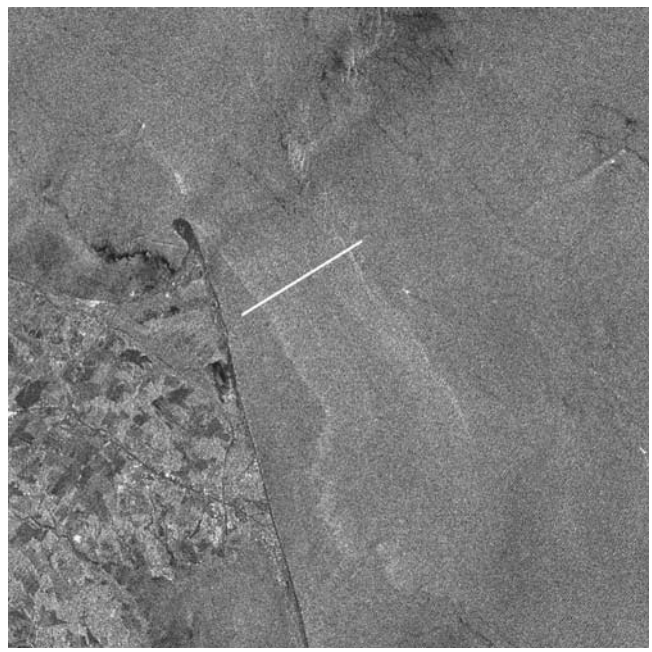

Figure 13. An ERS-2 standard image covering the Delaware Bay mouth region taken on 14 May 1997, 1543 UTC. The white line represents the transect along which gray level values are taken.

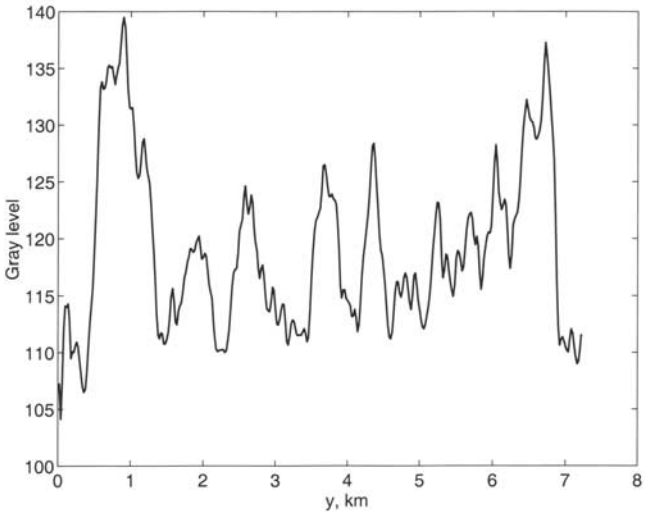

Figure 14. A curve of gray level values taken along white transect marked on Figure 13.

be divided into only two sections: (1) a width-unchanged section characterized by generally parallel image fronts and an almost unchanged transverse width of 3.2 km, and (2) a width-changed section characterized by a sharp width expansion to a maximum value of 5.3 km, and a gradually shrinking width as well as a less defined imaging of the front. If we assume the plume axis is parallel to the fronts of the width-unchanged section, the axis angle would be 17° relative to the coastline, which is an additional 7° shoreward when compared to the summer case.

[35] Unlike the summer and winter cases, image 97514 shows the plume as an integrated body with relatively uniform bright tunes. This may be explained by spring being the peak period for fresh water discharge in the Delaware Bay. The salinity of seawater in the plume therefore takes the lowest values of the year, which may reach as low as 26 psu or as much as 6 psu lower than surrounding continental shelf water [*Münchow and Garvine*, 1993a]. In this case, the salinity signals are intensive enough to overwhelm the current modulation signals. Figure 14 shows a curve representing the radar return intensity signals measured along transect marked by a white line on Figure 13. One can see that the twin fronts located on the two sides of the plume still generate strong radar return signals, but it is hard to determine the boundaries of the two jets within the plume. Hence we are unable to extract further information related to the jet dynamics from this image.

5. Conclusions and Discussion

[36] From the physics of radar imaging, ocean gravity-capillary wave spectra, and analytical solutions of a fluid jet, we derived theoretical model of a radar image for an ocean jet. If the effects of the ocean long waves are negligible, the theoretical model indicates that the jet radar image intensity depends strongly on the jet current structure and the sea surface wind direction with respect to the jet axis. The peak value of image intensity is dependent on the maximum axial velocity, while the position of the peak with respect to the axis depends on the wind direction. In all cases, the jet SAR image has a single peak.

[37] A twin jet physical model was used to describe the transverse current structure of Delaware Bay plume. The analysis indicated that this model not only conforms to field measurements and also explains the twin SAR image fronts.

[38] Interpretations of SAR images of the Delaware Bay plume from summer 1996 to spring 1997 indicate that in all seasons, low-salinity plumes appear as bright, jet-like patterns on the SAR images. As listed in Table 2, measurements give the axial length of the plumes at about 20 km and the transverse width varying from 3 km to 8 km. In summer and winter, the plumes can be divided into three sections along the axis: the source, jet, and dispersion sections. The typical axial velocity is estimated at 0.6 and 0.4 m s^{-1}, and the Reynolds number at 18 and 3, respectively. In spring, salinity signals overwhelm the current modulation signals, thus the plume appears as an integrated body with relatively uniform bright tunes on the SAR image.

[39] On the basis of the spreading of SAR image fronts, which, in fact, represent the streamlines, the physical natures of the plume jets can be determined. In summer, the jet behaves like a turbulent jet off the source region down to about 5 km downstream, and like a laminar jet from about 5 km down to about 10 km downstream. In winter, the jet behaves like a laminar jet off the source region down to about 4 km downstream.

[40] We note that the three analyzed cases of Delaware Bay plumes occurred at maximum flood tide or early flood tide of Delaware Bay entrance (Center for Operational Oceanographic Products and Services, 2004). This implies that countercurrents against the general tidal inflows formed the plumes. Although this conclusion needs further justification, it is in fact highly possible. *Li* [2001] presented a 3D solution for tides in channels with arbitrary lateral depth variation. One of his conclusions is that the time of flood (ebb) in deep water lags that in shallow water, and the time of flood (ebb) on the surface lags that at the bottom. His conclusion provides a dynamical basis for our interpretations for Delaware Bay plumes, which occur on the surface layer of a narrow and deep channel. It is the longest flood

Table 2. Seasonal Variability of Delaware Bay Plumes Derived from SAR Image Interpretation

	Summer	Winter	Spring
Date	13 Aug. 1996	7 Feb. 1997	14 May 1997
Tide[a]	maximum flood	maximum flood	early flood
Wind speed,[a] m s^{-1}	9.2	3.9	5.1
Wind dir.[a] with jet	135°	0°	135°
Plume width: source region, km	3.0	3.6	3.9
Plume width: Maximum, km	7.7	6.6	6.6
Axial dir. with coastline	23°	26°	17°
Axial length of plume, km	21.3	19.7	23.1
Length of source and jet, km	11.0	8.0	13.7
Axial velocity, m s^{-1}	0.6	0.4	N/A
Length scale, km	3	0.8	N/A
Reynolds number	18	3	N/A
Nature of jet	turbulent/laminar	laminar	N/A

[a]Field data.

time lag to maintain the existence of Delaware Bay plumes as a countercurrent. Furthermore, we have examined ADCP data collected in the same region by *Wong and Münchow* [1995] and found a regular distribution of the largest noise vectors with amplitudes of the order of 60 cm s^{-1} and downstream orientations at the deep channel [see *Wong and Münchow*, 1995, Figure 17c]. This seems to further indicate that outflow at the deep channel may always exist without regard to the tide stage.

[41] The case studies demonstrate that the methodology developed in this study can be used to establish the relationship between SAR signal and flow field. Therefore there should be potential applications to a wide range of problems.

[42] **Acknowledgments.** This work was partially supported by NOAA (NA17EC2449), NOAA Sea Grant Program (NA96RG0029), NASA (NAG5-13636 and NAG5-11773), and ONR-Physical Oceanography Program. We thank Zhongxiang Zhao for his help in processing the data.

References

Clemente-Colón, P. (2001), Coastal oceanography applications of space-born synthetic aperture radar (SAR) in the Middle Atlantic Bight (MAB), Ph.D. diss., 231 pp., Univ. of Delaware, Newark.

Garvine, R. W. (1991), Subtidal frequency estuary-shelf interaction: Observations near Delaware Bay, *J. Geophys. Res.*, *96*, 7049–7064.

Klein, L. A., and C. T. Swift (1977), An improved model for the dielectric constant of sea water at microwave frequencies, *IEEE Trans. Antennas Propag.*, *25*, 104–111.

Kundu, P. K. (1990), *Fluid Mechanics*, pp. 478–481, Academic, San Diego, Calif.

Li, C. (2001), 3D analytic model for testing numerical tidal models, *J. Hydrol. Eng.*, *127*, 709–717.

Münchow, A., and R. W. Garvine (1993a), Dynamical properties of a buoyancy driven coastal current, *J. Geophys. Res.*, *98*, 20,063–20,077.

Münchow, A., and R. W. Garvine (1993b), Buoyancy and wind forcing of a coastal current, *J. Mar. Res.*, *51*, 293–322.

Münchow, A. K., R. W. Garvine, and T. F. Pfeiffer (1992), Subtidal currents from a shipboard acoustic Doppler current profiler in tidally dominated waters, *Cont. Shelf Res.*, *12*, 499–515.

Plant, W. J. (1990), Bragg scattering of electromagnetic waves from the air/sea interface, in *Surface Waves and Fluxes*, vol. II, *Remote Sensing*, edited by G. L. Geernaert and W. J. Plant, pp. 41–108, Kluwer Acad., Norwell, Mass.

Polis, D. F., and S. L. Kupferman (1973), *Physical Oceanography, Delaware Bay Report Series*, vol. 4, pp. 1–143, Univ. of Delaware, Newark.

Sanders, T. M., and R. W. Garvine (1996), Frontal observations of the Delaware Coastal current source region, *Cont. Shelf Res.*, *16*, 1009–1021.

Saxton, J. A., and J. A. Lane (1952), Electrical properties of sea water, *Wireless Eng.*, 269–275.

Wong, K.-C., and A. Münchow (1995), Buoyant forced interaction between estuary and inner shelf: Observation, *Cont. Shelf Res.*, *15*, 59–88.

Yuan, Y. (1997), Representation of high frequency spectra of ocean waves and the basis for analyzing SAR images, *Chin. J. Oceanol. Limnol.*, *28*, suppl., 1–5.

Zheng, Q., X.-H. Yan, and V. Klemas (1993), Derivation of Delaware Bay tidal parameters from space shuttle photography, *Remote Sens. Environ.*, *44*, 1–10.

Zheng, Q., X.-H. Yan, V. Klemas, C.-R. Ho, N.-J. Kuo, and Z. Wang (1998), Coastal lee waves on ERS-1 SAR images, *J. Geophys. Res.*, *103*, 7979–7993.

Zheng, Q., Y. Yuan, V. Klemas, and X.-H. Yan (2001), Theoretical expression for an ocean internal solution SAR image and determination of the soliton characteristic half width, *J. Geophys. Res.*, *106*, 31,415–31,423.

P. Clemente-Colón, NOAA/NESDIS, E/RA3, Room 102, WWBG, 5200 Auth Road, Camp Springs, Maryland, USA.

N. E. Huang, Ocean and Ice Branch, NASA Goddard Space Flight Center, Greenbelt, Maryland, USA.

W. T. Liu, Jet Propulsion Laboratory 300-323, California Institute of Technology, Pasadena, California, USA.

X.-H. Yan, College of Marine Studies, University of Delaware, Newark, Delaware, USA.

Q. Zheng, Department of Meteorology, University of Maryland, College Park, Maryland, USA. (quanan@atmos.umd.edu)